Sensors and Materials, Vol. 37, No. 9 (2025) 4141–4163
MYU Tokyo

S & M 4173

Application of Image Recognition Technology in Mechanical Bearing Damage Detection

Chiu-Chang Chen,[1] Jenn-Kai Tsai,[2*] Wei-Ming Huang,[2] and Yan-Feng Wang[2]

[1]Doctoral Degree Program in Smart Industry Technology Research and Development, College of Engineering, National Formosa University, Yunlin 632, Taiwan
[2]Department of Electronic Engineering, National Formosa University, Yunlin 632, Taiwan

(Received March 31, 2025; accepted August 27, 2025)

Keywords: vibration, YOLOv7, image recognition, automatic identification

In this study, we aim to develop an automatic identification and diagnostic system for motor vibrations based on image processing technology. This technology converts motor time-domain vibration signals, acquired from a single-axis accelerometer, into original frequency-domain signals and performs multilevel smoothing processing to generate energy trend spectral graphs. These graphs are used to reduce the computational load for image recognition and improve its accuracy. Subsequently, you only look once version seven (YOLOv7) image processing model is used for establishment and training. The established system automatically identifies mechanical vibration modes. Digital band-pass filtering technology is also used to select a single mechanical vibration mode for analysis. Next, the cumulative enhanced energy operator (CEEO) is used to demodulate the original signal, generating CEEO signals. By analyzing the CEEO spectrum and motor bearing damage characteristics, the health status of the motor is determined. By using AI in this system, the labor and long-term training costs of personnel can be reduced, ensuring the appropriate functioning of critical components.

1. Introduction

Modern manufacturing focuses on automated production to save labor costs, increase production speed, and improve product quality. In such automation, consumable parts such as motors and gearboxes are widely used, and the failure of these parts leads to production line shutdowns and endangers personnel safety.[1–4] Motor bearings are one of the most commonly used components in automated production systems, so it is important to monitor their status in real time.

At present, a prevalent approach to bearing diagnosis is high-frequency demodulation analysis. However, one of the challenges preventing the effective automation of this method is the reliance on professionals to identify vibration resonance modes. These modes are excited at different frequencies as the rotational speed changes, as shown in Fig. 1. This process is time-

*Corresponding author: e-mail: tsaijk@nfu.edu.tw
https://doi.org/10.18494/SAM5675

ISSN 0914-4935
https://myukk.org/

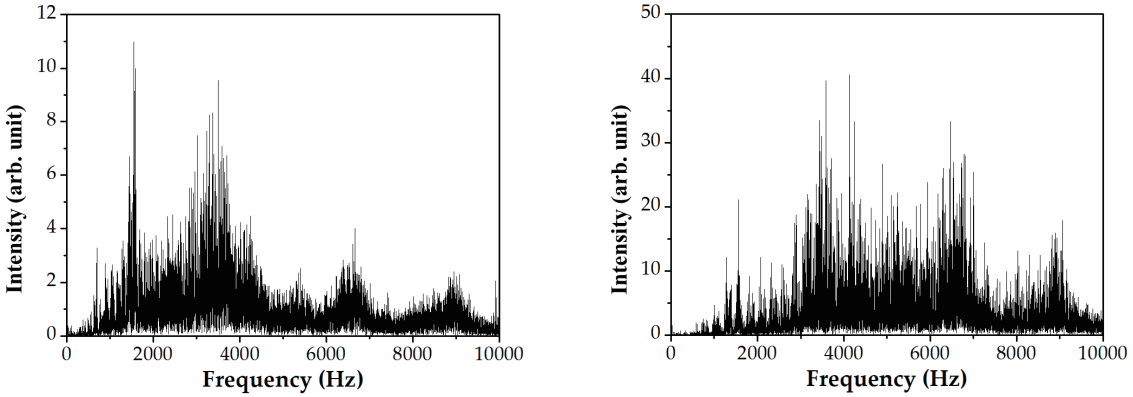

Fig. 1. Frequency spectra of the same damaged bearing operating at (a) 800 and (b) 1600 rpm.

consuming and heavily dependent on expert knowledge.[5,6] In practice, many motor applications involve nonfixed rotational speeds.

In recent years, AI has experienced rapid growth, with significant breakthroughs in machine learning and its applications across various industries. Among these, image recognition technology has emerged as one of the most widely adopted techniques. In this study, image recognition was employed to analyze vibration modes, thereby reducing reliance on expert judgment and enabling automated analysis.

Therefore, we propose a novel method for automatically identifying mechanical resonance modes. Once vibration modes can be automatically and quickly identified, the problem of fluctuating resonance modes in variable-speed motor systems can be effectively resolved.

In this study, fast Fourier transform (FFT) and simple moving average (SMA) were used for signal preprocessing to reduce computational load. We also used you only look once version seven (YOLOv7) for automatic mode selection. The selected modal frequency bandwidth was then subjected to band-pass filtering, followed by cumulative enhanced energy operator (CEEO) demodulation. The process can be used to identify the characteristic frequency of a damaged bearing. Image recognition is currently one of the most important research topics, with a wide range of applications.[7,8] In this study, we used image recognition for automatic mode selection to automate the process of bearing damage identification. YOLOv7 was selected as the model for this study because it offers higher processing speed and accuracy than previous versions of YOLO,[9–11] making it the preferred choice for this research. Since the raw vibration time-domain signals are highly complex and may negatively affect the training performance of the YOLO model, signal preprocessing was performed using FFT and SMA to reduce computational load and improve training effectiveness.

Researchers are actively seeking new solutions. In this study, we propose a technology that focuses on automatic mode identification rather than signal demodulation. Before signal demodulation can be performed, it is necessary to first identify the resonance mode. Once the resonance mode is identified, the modal signal can be extracted through band-pass filtering and subsequently demodulated to reveal the damage characteristic frequency. One commonly used

demodulation technique is wavelet analysis; however, it requires significant computational resources, making it unsuitable for widespread application in embedded systems.[12,13] Additionally, the hardware costs associated with wavelet analysis are relatively high.

In recent years, studies have introduced CEEO, a lightweight analysis technique capable of delivering results comparable to wavelet analysis but with significantly lower computational demands.[14,15] Therefore, we adopted CEEO for modal signal demodulation, aiming to advance automated diagnostic technology. The demodulated signal must correspond to the characteristic frequencies calculated for different bearing damage locations and rotational speeds.

The accuracy of the automatic modal identification technology proposed in this study hinges on its ability to accurately identify modal patterns. The integrity of the bearings was intentionally compromised using electrical discharge machining with known damage locations, ensuring the reliability of the damage results obtained through demodulation. Conversely, if the identified modal patterns prove to be inaccurate, no damage characteristic frequencies will be observed after demodulation.

We integrated FFT, band-pass filtering, SMA, image recognition, and CEEO demodulation to develop an automated bearing damage detection system. Compared with the existing approaches proposed by other researchers, the proposed method achieves automated bearing damage assessment with significantly lower computational requirements.

2. Methods

In this study, image processing technology for graphical recognition processing was used for the automatic mode selection and recognition of vibrations. The vibration signals of mechanical bearings were obtained using a graphical recognition model.

Figure 2 shows the system validation process. First, the original vibration signal is obtained using a single-axis accelerometer. Signal processing is then performed by converting the time domain signal to the frequency domain signal using FFT and then smoothing the signal using the SMA method. The processed image is then fed into the trained automatic recognition model to obtain the mode frequency band. The identified mode frequency band is set as the region of the digital bandpass filter to block components with frequencies above or below this band. The original vibration spectrum is simplified to the new one. This is followed by demodulation using CEEO to obtain the characteristic frequency of the damaged bearing. Finally, this frequency is compared with the characteristic frequencies to verify the accuracy of the model's prediction.

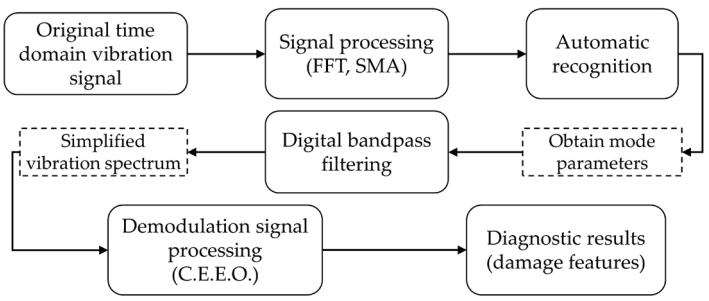

Fig. 2. Illustration of workflow for validating the bearing damage diagnostic system.

The model automatically identifies vibration modes. The accuracy of the model in training does not necessarily represent its recognition ability of vibration modes.[16] Therefore, the model must be tested to verify its recognition ability. In this case, a confusion matrix is used to present the recognition results as shown in Table 1. The measures of the confusion matrix are as follows.

- *TP* (True Positive): Correctly predicting the positive class as positive
- *FN* (False Negative): Incorrectly predicting the positive class as negative
- *FP* (False Positive): Incorrectly predicting the negative class as positive
- *TN* (True Negative): Correctly predicting the negative class as negative

Precision, recall, and F1 score are used to evaluate the performance of the neural network model.

Precision: This metric is used to evaluate the recognition accuracy of individual classifications.

$$\text{Precision} = \frac{TP}{(TP + FP)} \tag{1}$$

Recall: This metric represents the proportion of instances of a particular true class that is successfully recognized.

$$\text{Recall} = \frac{TP}{(TP + FN)} \tag{2}$$

F1 score: This metric represents the harmonic means of precision and recall. The closer its value to 1, the higher the recognition accuracy of the model.

$$\text{F1 score} = 2 \times \frac{(Precision \times Recall)}{(Precision + Recall)} \tag{3}$$

In addition to the confusion matrix, the mean average precision (mAP) is also used to evaluate the performance of the model. mAP represents the average precision (AP) of all categories of vibration modes. AP represents the recognition performance by calculating the area under the precision-recall curve. To compute mAP, AP for each category is calculated and then averaged to obtain mAP. mAP is classified on the basis of different intersections over union (IoU). Common reference values include mAP@0.5 (IoU threshold of 0.5), mAP@0.95 (IoU threshold of 0.95), and mAP@0.5:0.95 (averaging AP values over IoU thresholds from 0.5 to 0.95 with a step of 0.05). In this study, since there is only one category, mAP is equal to AP.[17–20]

Table 1
Confusion matrix table with four different combinations of predicted and actual values.

Confusion matrix		Actual value	
		Positive	Negative
Predicted value	Positive	*TP*	*FP*
	Negative	*FN*	*TN*

The image recognition model requires the vibration spectrum as training data, with features marked in the spectrum. However, the vibration spectral graph is complex with nonmodal energy peaks that cause recognition errors. Therefore, we simplified the graph and smoothed out the nonmodal high-energy signals that lead to false detections to automatically identify vibration modes. As a result, the SMA method was adopted. This method suppresses high-energy peaks and amplifies less notable energy, thereby increasing the success rate of mode recognition [Eq. (4)].

$$SMA = \frac{C_1 + C_2 + C_3 + C_4 + C_5 + ... + C_n}{n} \tag{4}$$

Here, C represents the energy values at different frequencies and n represents the total number of frequencies in the processed spectrum pattern.[21,22]

3. Theoretical Analysis of Bearing Damage

The bearing signal analysis method used in this system is CEEO. This method analyzes a single-mode vibration signal using a bandpass filter and the CEEO signal spectrum to determine whether the bearing exhibits characteristic frequencies of damage.[14,15] As the frequency band captured in this method is in the high frequency range, low-frequency noise can be filtered out, reducing the noise of the signal. In a damaged bearing system, the failure of any component, regardless of the specific damage morphology, generates a corresponding vibration signal, and the analysis of the demodulated spectrum reveals the characteristic frequency associated with the damaged component. Equations (5) to (7) are used to calculate characteristic frequencies in four different damage scenarios.[23–25]

$$\text{Damaged inner ring characteristic frequency, } f_{in}\text{: } f_{in} = \frac{N}{2} f_{rpm}\left(1 + \frac{d}{D}\cos\varphi\right) \tag{5}$$

$$\text{Damaged roller characteristic frequency, } f_{roll}\text{: } f_{roll} = \frac{D}{d} f_{rpm} = \left[1 - \left(\frac{d}{D}\right)^2 \cos^2\varphi\right] \tag{6}$$

$$\text{Damaged outer ring characteristic frequency, } f_{out}\text{: } f_{out} = \frac{N}{2} f_{rpm}\left(1 - \frac{d}{D}\cos\varphi\right) \tag{7}$$

Here, f_{rpm} is the true frequency of shaft rotation, D is the pitch diameter of the bearing, d is the diameter of the rolling elements, N is the number of rolling elements in the bearing, and φ is the contact angle of the rolling elements.

In this study, we artificially created defects on the inner ring, roller, and outer ring of the bearing using electrical discharge machining. The damaged bearing was then operated at 800, 1600, and 2400 rpm, and its vibration signals were recorded. The defect characteristic

frequencies of the damaged bearing were calculated using Eqs. (5)–(7), and the calculated values are shown in Table 2.

The accuracy of the model's predictions was verified by comparing the results obtained from image recognition at the characteristic frequencies shown in Table 2. In a bearing, the carrier signal is a combination of the resonant frequencies of the bearing or the entire system. Therefore, the amplitude-modulated vibration signal v(t) is expressed as[26–29]

$$v(t) = \sum_{l=1}^{L}\left(\sum_{m=1}^{md}\int_{-\infty}^{t} d_m(\tau)q_m(\tau)a_{lm}(\tau)e^{-\sigma_l(t-\tau)}\cos(2\pi f_l(t-\tau)+\theta_{lm})d\tau + \sum_{n=1}^{n_r}\int_{-\infty}^{t} g_n(\tau)q_n(\tau)a_{ln}(\tau)e^{-\sigma_l(t-\tau)}\cos(2\pi f_l(t-\tau)+\theta_{ln})d\tau + \omega(t)\right). \quad (8)$$

The three summation terms in Eq. (8) represent the vibrations from defective and normal components, and low-frequency mechanical noise $\omega(t)$. In the first term, m_d stands for the number of damages and $d_m(t)$ is the modulating signal, which represents the damage impulse train. $q_m(t)$ provides information about the damage dimensions and the sensitivity to impact energy, while $a_{lm}(t)$ is the characteristic function of the transmission path. The second term is related to normal components, where n_r is the number of rollers and $g_n(t)$ describes the surface functions of the normal bearing components for each roller. $q_n(t)$ represents the equivalent stiffness of roller n and $a_{ln}(t)$ is the transmission path function, which determines the vibration intensity excited by roller n. The variables σ_l and f_l are the exponential decay and carrier frequencies, respectively, which represent structural characteristics of the system. L is the number of resonance modes, whereas θ_{lm} and θ_{ln} are the initial angles for amplitude modulation.[29]

We assume that the impulse responses from $d_m(t)$ decay completely within the time interval between two consecutive contacts, and that the resonance frequency f_l is high. The energy from surface irregularities $g_n(t)q_n(t)$ is much smaller than that from bearing defects. Therefore, the second summation term in Eq. (8) can be ignored, simplifying the vibration signal as follows.

$$v(t) = \sum_{l=1}^{L}\left(\sum_{m=1}^{md} u_m(t)q_m(t)a_{lm}(t)\cos(2\pi f_l t+\theta_{lm})\right) \text{ with } u_m(t) = e^{-\sigma_l(t')},\ t' = \mathrm{mod}(t, 1/f_{dm}) \quad (9)$$

Here, mod($1/f_{dm}$) represents a remainder of t and f_{dm} is the frequency of impulse train $d_m(t)$.

A new method for processing bearing signals, derived from traditional energy processing methods, was proposed by Liang and Bozchalooi.[25] To analyze the energy characteristics of the signal, the energy operator of the vibration signal function $\psi(g(t))$ is used as

Table 2
The characteristic frequencies of damaged bearings were calculated at three different speeds and locations.

Rotation speed (rpm)	2400	1600	800
Feature frequency of damaged inner ring, f_{in} (Hz)	395.2	263.5	131.7
Feature frequency of damaged roller, f_{roll} (Hz)	233.6	155.7	77.9
Feature frequency of damaged outer ring, f_{out} (Hz)	284.8	189.9	94.9

$$\psi(g(t)) = \left(\frac{d}{dt}g(t)\right)^2 - g(t)\frac{d^2}{dt^2}g(t). \tag{10}$$

This method is commonly used in the frequency and amplitude modulation of speech signals. On the basis of its characteristics, the transient signals of damaged impulses are analyzed with frequency and amplitude modulation characteristics. Therefore, it is assumed that vibration signals are arbitrary signals with frequency and amplitude modulation characteristics, as follows:

$$g(t) = f(t) \cdot \cos(\varphi(t)), \tag{11}$$

where $f(t)$ is its amplitude variation function over time.

For the analysis of discrete signal $D(g(n))$, since the sampling frequency is 1 Hz, assuming $\Delta t = 1$ s, its differential expression at time n can be represented as

$$D(g(n)) = [g(n) - g(n - \Delta t)] / \Delta t = g(n) - g(n-1). \tag{12}$$

Therefore, the discrete-time representation of the vibration signal $y(g(n))$ is

$$\begin{aligned} y(g(n)) &= Dg(n)^2 - g(n)D(Dg(n)) \\ &= g(n-1)^2 - g(n)g(n-2). \end{aligned} \tag{13}$$

When the variable $m = n - 1$, the above equation is reformulated as

$$y(g(m)) = g(m)^2 - g(m+1)g(m-1)). \tag{14}$$

In addition, when performing signal integration in discrete form $I(g(n))$, the trapezoidal rule is used to save computation time.

$$I(g(n)) = \Delta t[g(n) + g(n - \Delta t)] / 2 \tag{15}$$

If we assume $\Delta t = 1$ s, the integral expression is simplified to

$$I(g(n)) = [g(n) + g(n - \Delta t)] / 2. \tag{16}$$

Differentiation enhances the signal-to-interference ratio, while integration improves the signal-to-noise ratio.[15] Therefore, by defining a layer operator (LO) that includes differentiation and integration operations, the advantages of both can be maximized. Therefore, the first-layer operator analysis of the vibration signal can be defined by the function $g(t)$ as follows:

$$\begin{aligned} LO_1(g(n)) &= I(Dg(n)) \\ &= g(n) - g(n-2). \end{aligned} \tag{17}$$

By repeatedly applying layer operator analysis, we obtain the second-layer operator as

$$\begin{aligned} LO_2(g(n)) &= LO_1(LO_1(g(n))) \\ &= g(n) - 2g(n-2) + g(n-4). \end{aligned} \tag{18}$$

Similar to the energy operator analysis method, replacing the original first and second derivatives with the first and second-layer operators allows for the following equation:

$$CEEO(g(m)) = LO_1(g(n))^2 - g(n)LO_2((gn)). \tag{19}$$

4. Experimental Equipment

To validate the developed bearing damage diagnosis system, we set up an experimental apparatus, as shown in Fig. 3 and Table 3. Since the same bearing exhibits different vibration modes at different rotational speeds, the apparatus included a motor speed controller. The motor was connected to a rotating shaft through a coupling, which was then linked to the high-speed

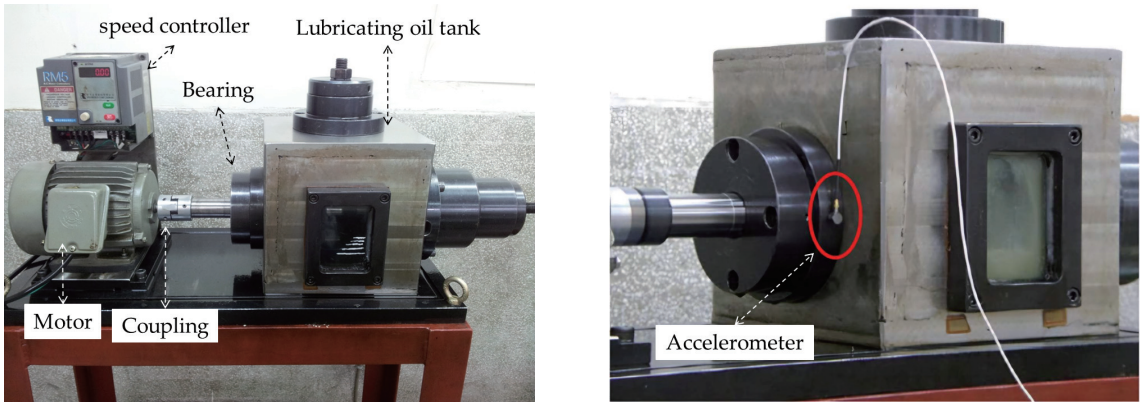

(a) (b)

Fig. 3. (Color online) Diagram of bearing testing machine. (a) Image of bearing testing machine. (b) Position of accelerometer.

Table 3
The characteristic frequencies of damaged bearings were calculated at three different speeds and locations.

Components	Model
Drive motor	TECO three-phase motor
Motor controller	rhymebus RM5-2005
Test bearing	32208 Single row tapered roller bearing
Data acquisition	NI 9215
Accelerometer	PCB 352C68

headstock. A lubrication system was also integrated. In addition to the mounted bearing mechanism, a single-axis accelerometer was installed to measure the vibration signal. In this study, the sampling rate was set to 100 kHz, with a sampling time of 1 s, resulting in a total of 100k samples. The control, data acquisition, and computation of the acquisition card were all performed using MATLAB 2014A.

In the experiment, we used electrical discharge machining technology to simulate bearing damage. We intentionally machined defects on the inner ring, roller, and outer ring, as shown in Fig. 4.

The damaged area of the bearing was examined under a microscope, revealing a 0.2-mm-wide trace on the inner ring, as shown in Fig. 5, and the damaged parameters are shown in Table 4.

(a) (b) (c)

Fig. 4. (Color online) Bearing with damaged parts caused by electrical discharge machining. The linear damage is highlighted in circles. (a) Inner ring, (b) roller, and (c) outer ring.

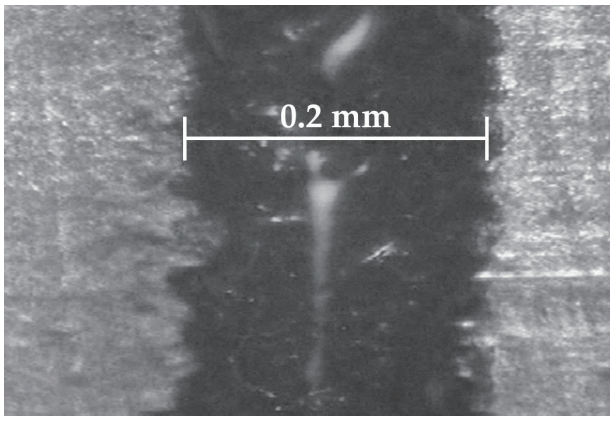

Fig. 5. Optical microscopy image of the damaged inner ring.

Table 4
Damage size of bearing.

Damaged parts	Damage size ([length (mm) × width (mm) × depth (mm)]
Inner ring	14.0 × 0.15 × 0.2
Roller	16.0 × 0.15 × 0.2
Outer ring	18.5 × 0.15 × 0.2

We ran the model on a computer equipped with NVIDIA GeForce RTX4070 (graphics processing unit) with 5888 CUDAs and 12 GB of video memory. The central processing unit was Intel(R) Core (TM) i7-14700. The operating system was Windows 10, and PyTorch version 2.20, Python version 3.10, and CUDA version 12.5 were used.

5. Current Results

Figure 6 shows the signal process workflow for model training. First, we measured the vibration signal using a single-axis accelerometer. To make the signal easier to analyze, we converted the time-domain signal into the frequency-domain signal using FFT. Since the original frequency spectrum signal does not perform well for image recognition training, we processed it with SMA to improve effectiveness.

To train the automatic vibration mode recognition model, we processed the original frequency domain signal (Fig. 7) by the SMA method. We applied SMA calculation every 100 data points on the signal to produce a smoothed energy distribution graph, and we manually determined the

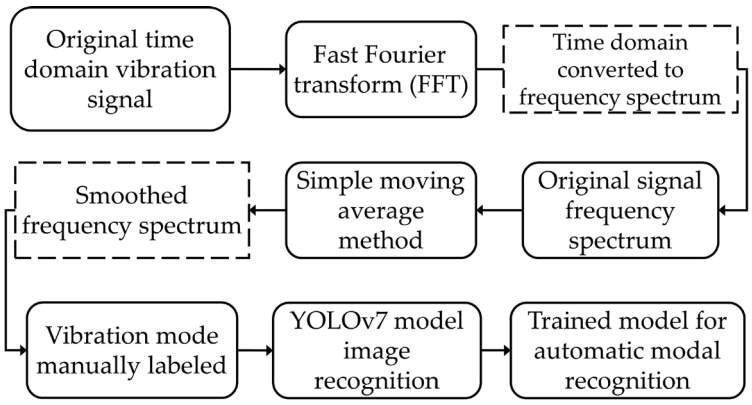

Fig. 6. Illustration of signal processing workflow for image recognition model training.

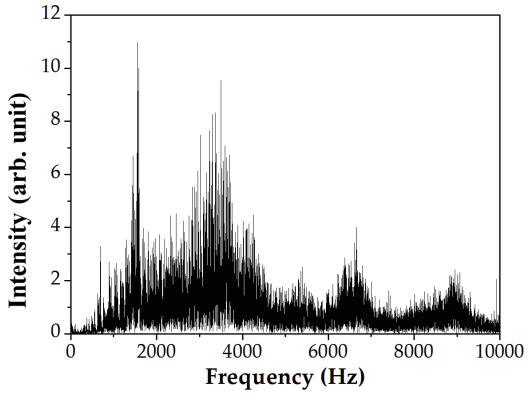

Fig. 7. Frequency domain signal of damaged inner ring bearing at 800 rpm.

vibration mode positions (Fig. 8). A total of four vibration modes were identified in the energy plot. The dataset included 951 images, similar to Fig. 7, which were used to train the model with YOLOv7, resulting in an AI model capable of automatically recognizing vibration modes. The vertical axis unit "arb. unit" in the figure represents an arbitrary unit.

The dataset contained 951 images of vibration spectra at 800, 1600, and 2400 rpm. We used 70% of the data for training and 30% for validating, resulting in 666 and 285 images, respectively. We trained the model for 50 epochs with a batch size of 8 and set the image dimensions to 640 × 640 pixels.

Figure 9 shows the confusion matrices of the model, which we used to evaluate the model's performance. The top left corner indicates *TP*, the top right corner indicates *FP*, the bottom left corner indicates *FN*, and the bottom right corner indicates *TN*. The model shows an excellent *TP* score of 0.97, indicating that it successfully identifies modal features. The *FP* score is 1.00

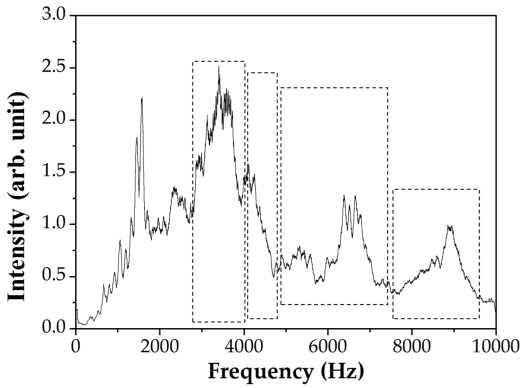

Fig. 8. Frequency domain signal after SMA processing and manual labeling of resonance features (dashed rectangle).

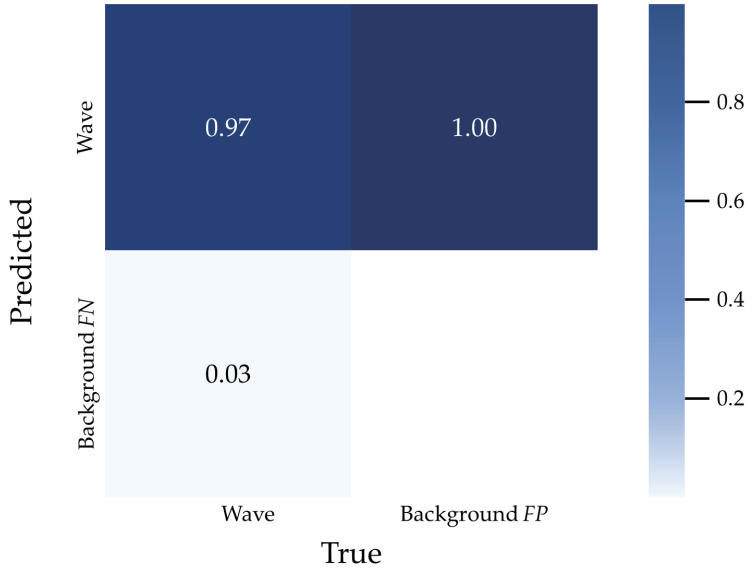

Fig. 9. (Color online) Confusion matrices of the model, which evaluates its performance.

because the model is designed for single-class detection with a background, and there are no true negative samples for the background class in the validation set.

Table 5 and Fig. 10 show the performance evaluation metrics and their performance curves, respectively. The precision confidence curve shows a precision of 1.00 at a confidence level of 0.957, highlighting the model's accuracy in correct predictions. The recall confidence curve exhibits a recall of 0.99 at a confidence level of 0.000. mAP is 0.973 at a confidence level of 0.5, indicating the model's effectiveness in damage detection. The F1 score confidence curve indicates an F1 score of 0.97 at a confidence level of 0.423, reflecting a balance between precision and recall, showing that the model successfully identifies almost all positive instances.

After completing the training of the image recognition model, we carried out the verification process following the steps shown in Fig. 2 to determine whether the model can automatically select the correct modes from the original frequency-domain signal. First, we operated the

Table 5
Performance of YOLOv7 model.

Precision	Recall	F1 score	mAP@0.5	mAP@0.5:0.95
0.9769	0.9569	0.9667	0.973	0.7114

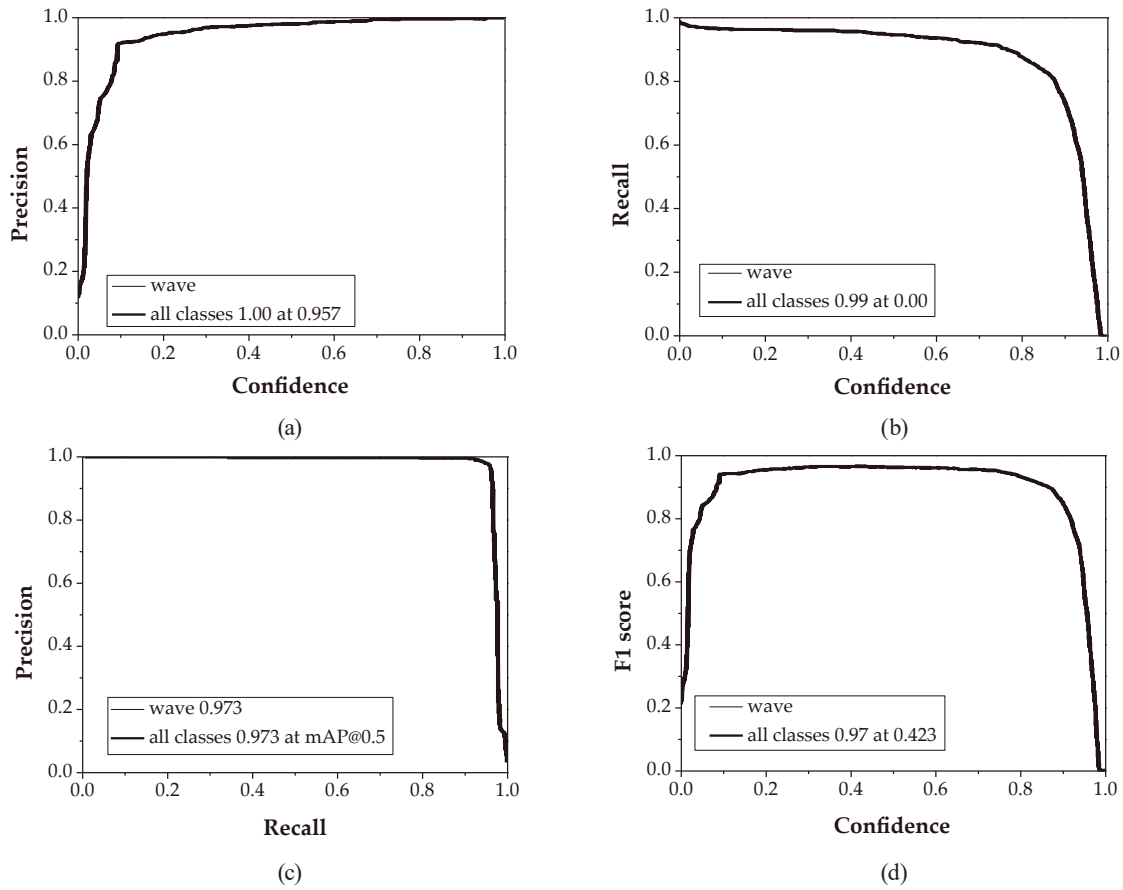

Fig. 10. Performance curves of the model. (a) precision confidence, (b) recall confidence, (c) precision–recall, and (d) F1 score confidence curves.

bearing with the damaged inner ring at 2400 rpm to acquire vibration signals, which we then converted into a frequency spectrum using FFT, as shown in Fig. 11. Next, we applied SMA processing, as shown in Fig. 12.

After processing the data by the SMA method, we used the trained model to perform mode recognition. The recognized spectrum is shown in Fig. 13, where the model automatically identifies two vibration modes. Next, we applied a digital band-pass filter to extract one of the vibration modes, and we programmed the AI model to select the mode. The lowest-frequency mode was selected by the model. The result with a band-pass filter to the original spectrum is shown in Fig. 14. The wave score indicates the similarity of the recognized vibration mode with the selected mode having a bandwidth of 4233 to 7716 Hz.

After bandpass filtering, we demodulated the spectrum using CEEO to obtain the characteristic frequency of the damaged bearing, as shown in Fig. 15. We compared this frequency with the results shown in Table 2 to verify the accuracy of the system analysis. The demodulated spectrum shows a characteristic peak at 396.1 Hz and a second harmonic at 792.1 Hz, which matches the calculated values shown in Table 2.

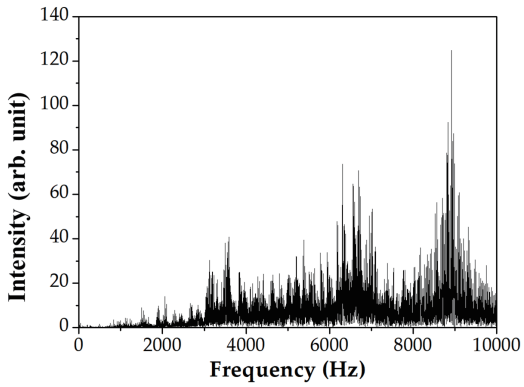

Fig. 11. Frequency domain spectrum of damaged inner ring bearing operating at 2400 rpm.

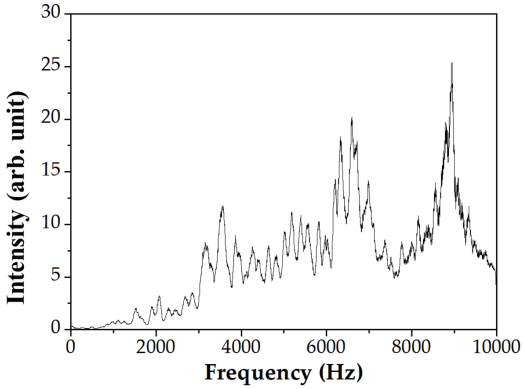

Fig. 12. Frequency domain spectrum of damaged inner ring bearing operating at 2400 rpm after the SMA process treatment is applied.

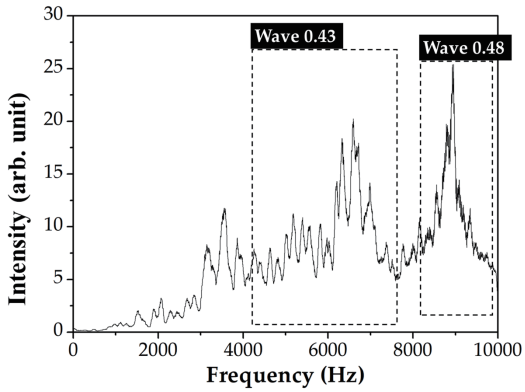

Fig. 13. Automatically selecting vibration mode with the trained model.

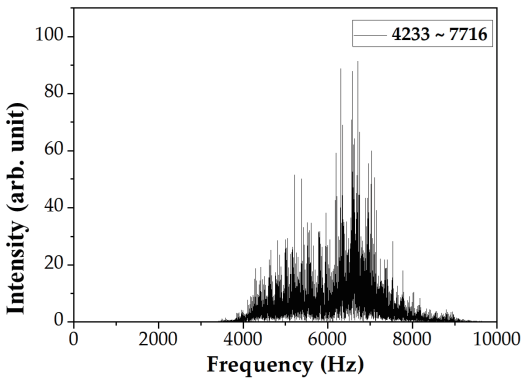

Fig. 14. Band-pass filtering was applied to the vibration signal of a damaged inner ring bearing operating at 2400 rpm.

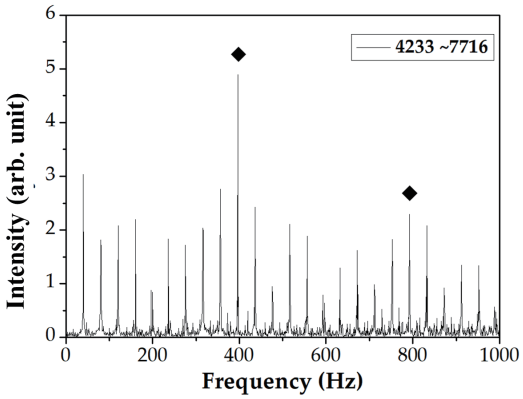

Fig. 15. After treatment with CEEO, the frequency spectrum of the damaged inner ring operating at 2400 rpm was obtained.

We operated the normal bearing at 2400 rpm. We measured its vibration signal and processed it using the automatic identification system, as shown in Fig. 16. When Figs. 16(a)–16(c) are compared with Figs. 11–14, the waveforms of both normal and damaged bearings, after FFT, SMA processing, and band-pass filtering, exhibit similar patterns. This similarity makes it difficult to determine whether the bearing is damaged and to identify the location of the damage. However, Fig. 16(d) shows that, compared with Fig. 15, the frequency spectrum after CEEO processing does not exhibit significant characteristic peaks or harmonics. This indicates that when a bearing is damaged, a significant signal intensity appears at the damage characteristic frequency. The overall frequency spectrum intensity of a normal bearing is very low, as shown in Fig. 16(d). Compared with Fig. 15, this significant difference allows us to determine whether the bearing is damaged on the basis of the strength of the characteristic peak.

To validate the model, normal bearings were operated at 800 and 1600 rpm, and their vibration signals were analyzed, as shown in Figs. 17 and 18. We processed the vibration signals obtained at these two rotational speeds through the automatic identification system, yielding results similar to those obtained at 2400 rpm. After applying CEEO signal demodulation, we did not observe significant damage characteristic peaks in any of the cases.

In addition to the normal bearings, we operated bearings with damage to other components (inner ring, roller, and outer ring) at 2400, 1600, and 800 rpm. We analyzed their vibration signals using the automatic identification system. As the analysis results for the damaged inner ring bearing operating at 2400 rpm have already been discussed, they will not be repeated here.

Figures 19 and 20 show the automatic identification results for bearings with damage to the roller and outer ring, respectively. Figures 21–23 show the automatic identification results for bearings with damage to the inner ring, roller, and outer ring, operating at 1600 rpm, respectively. Figures 24–26 show the automatic identification results for bearings with damage to the inner ring, roller, and outer ring, operating at 800 rpm, respectively.

On the basis of the results shown in Figs. 19–26, the characteristic frequencies identified by the automatic recognition system are compared with the calculated values shown in Table 2, as shown in Table 6. Table 6 shows that the values predicted using the automatic recognition system

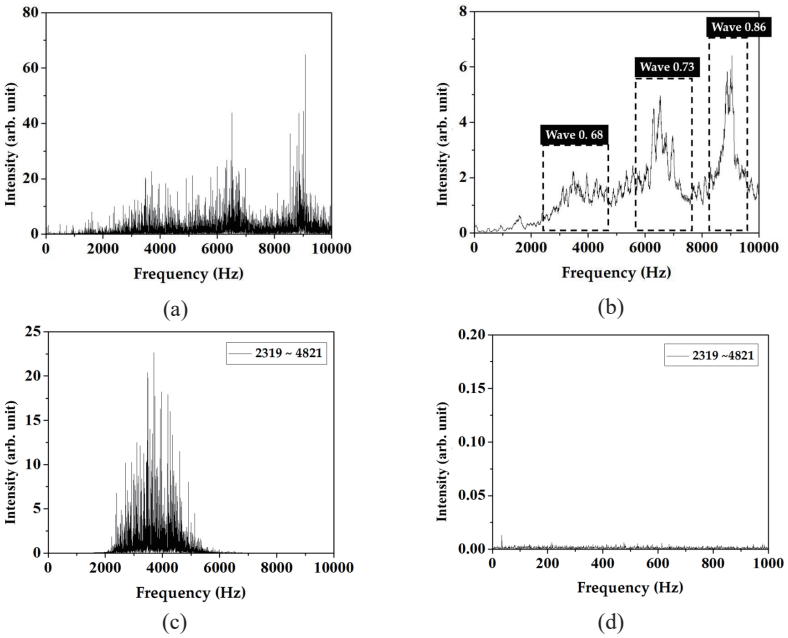

Fig. 16. Validation of bearing damage diagnostic system: frequency domain signal of (a) normal bearing operating at 2400 rpm, (b) applied SMA treatment and automatic mode selection, (c) after bandpass filtering, and (d) CEEO signal demodulation.

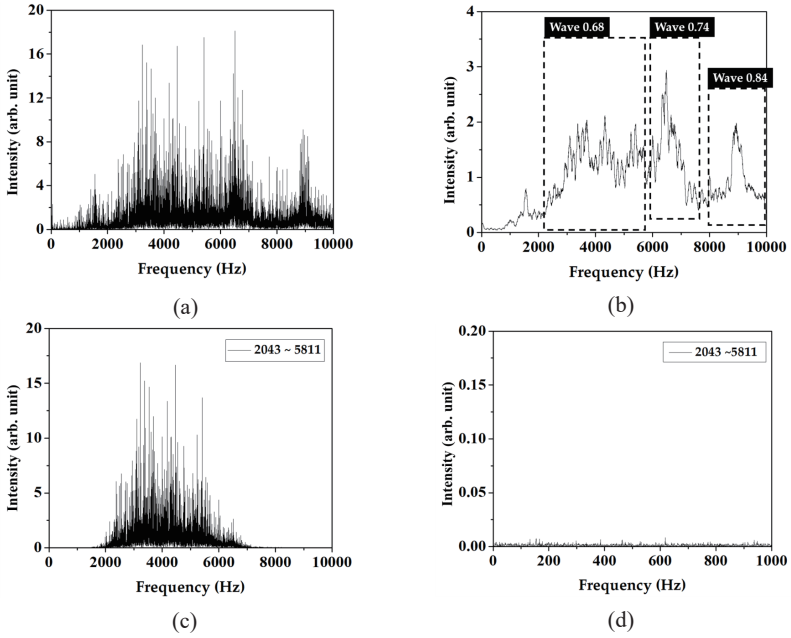

Fig. 17. Validation of bearing damage diagnostic system: frequency domain signal of (a) normal bearing operating at 1600 rpm, (b) applied SMA treatment and automatic mode selection, (c) after bandpass filtering, and (d) CEEO signal demodulation.

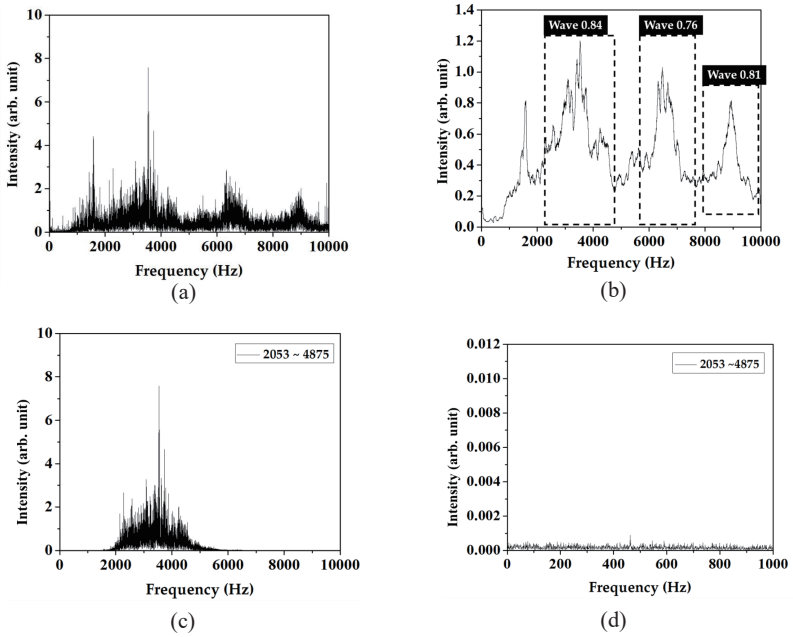

Fig. 18. Validation of bearing damage diagnostic system: frequency domain signal of (a) normal bearing operating at 800 rpm, (b) applied SMA treatment and automatic mode selection, (c) after bandpass filtering, and (d) CEEO signal demodulation.

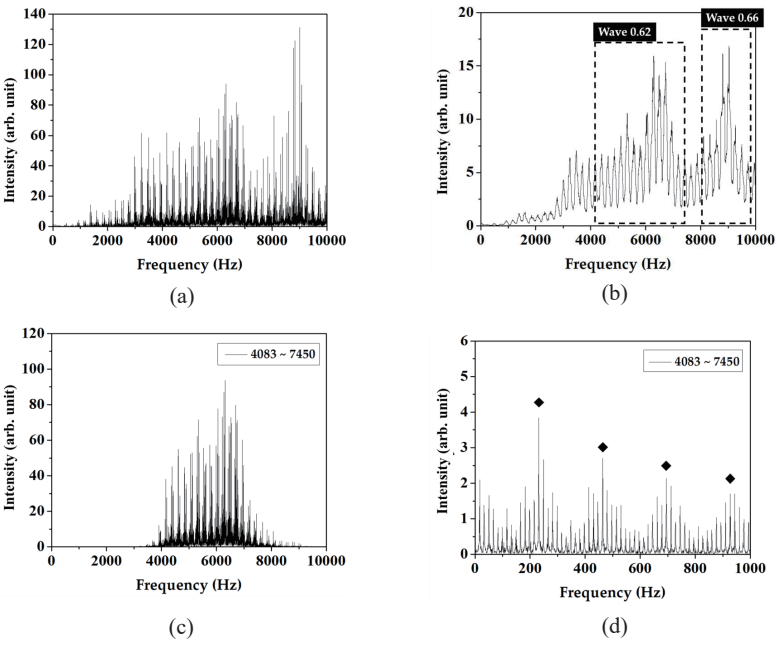

Fig. 19. Validation of bearing damage diagnostic system: frequency domain signal of (a) damaged roller bearing operating at 2400 rpm, (b) applied SMA treatment and automatic mode selection, (c) after bandpass filtering, and (d) CEEO signal demodulation.

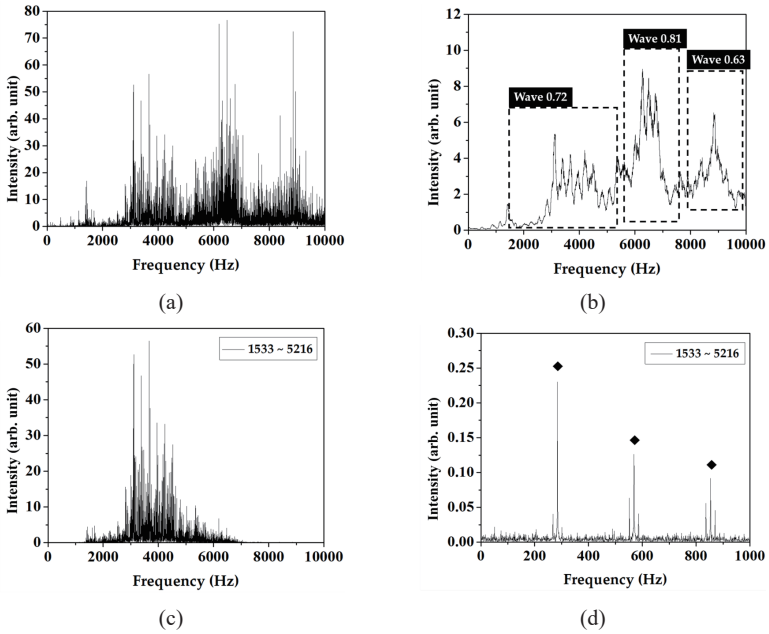

Fig. 20. Validation of bearing damage diagnostic system: frequency domain signal of (a) damaged outer ring bearing operating at 2400 rpm, (b) applied SMA treatment and automatic mode selection, (c) after bandpass filtering, and (d) CEEO signal demodulation.

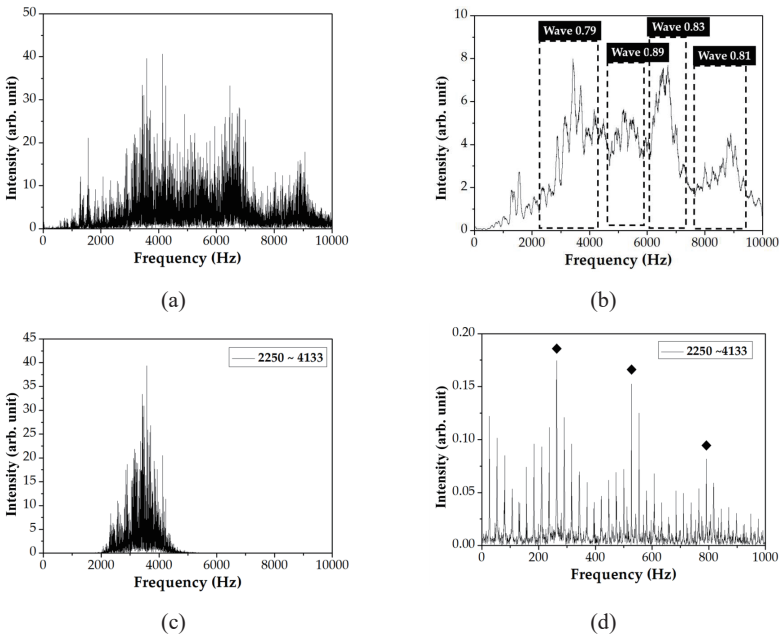

Fig. 21. Validation of bearing damage diagnostic system: frequency domain signal of (a) damaged inner ring bearing operating at 1600 rpm, (b) applied SMA treatment and automatic mode selection, (c) after bandpass filtering, and (d) CEEO signal demodulation.

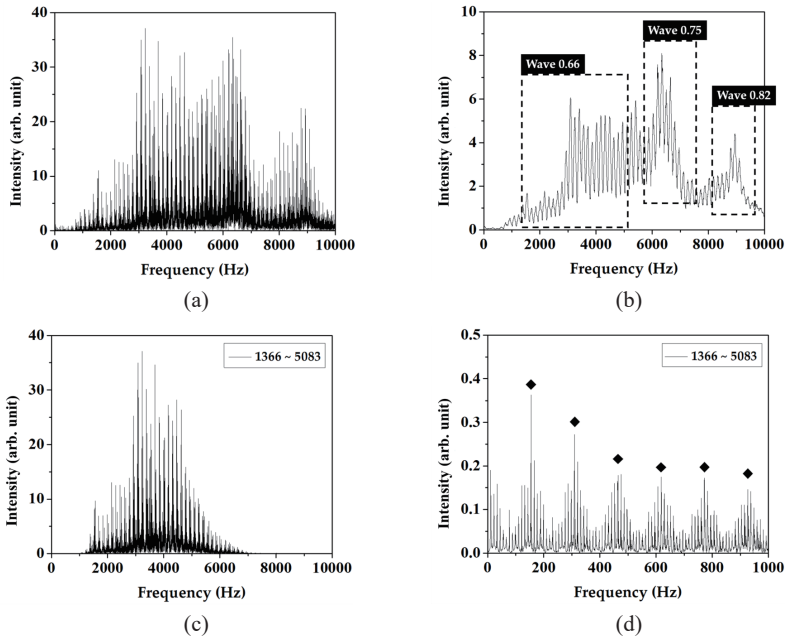

Fig. 22. Validation of bearing damage diagnostic system: frequency domain signal of (a) damaged roller bearing operating at 1600 rpm, (b) applied SMA treatment and automatic mode selection, (c) after bandpass filtering, and (d) CEEO signal demodulation.

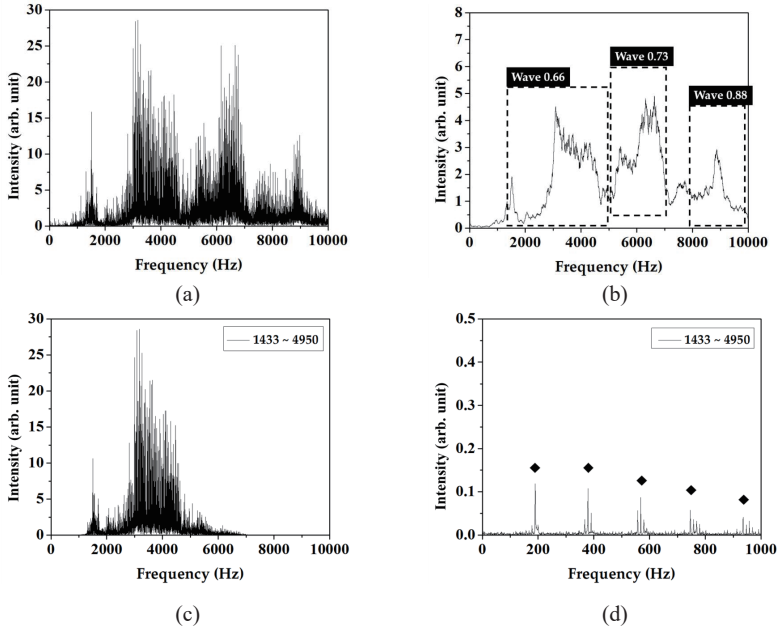

Fig. 23. Validation of bearing damage diagnostic system: frequency domain signal of (a) damaged outer ring bearing operating at 1600 rpm, (b) applied SMA treatment and automatic mode selection, (c) after bandpass filtering, and (d) CEEO signal demodulation.

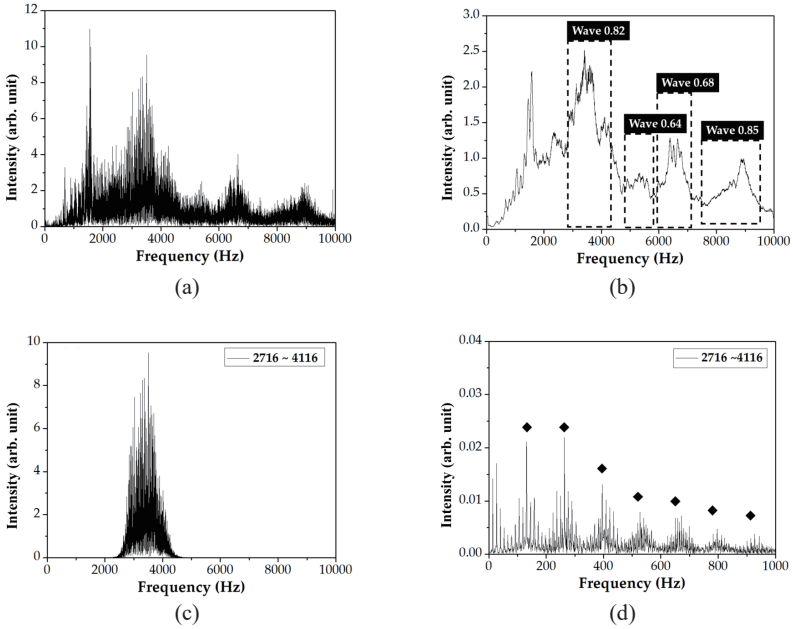

Fig. 24. Validation of bearing damage diagnostic system: frequency domain signal of (a) damaged inner ring bearing operating at 800 rpm, (b) applied SMA treatment and automatic mode selection, (c) after bandpass filtering, and (d) CEEO signal demodulation.

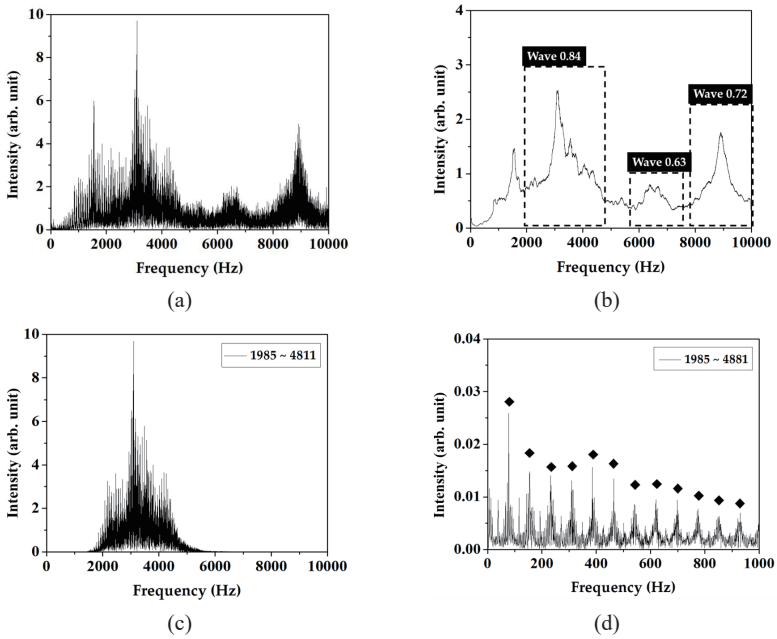

Fig. 25. Validation of bearing damage diagnostic system: frequency domain signal of (a) damaged roller bearing operating at 800 rpm, (b) applied SMA treatment and automatic mode selection, (c) after bandpass filtering, and (d) CEEO signal demodulation.

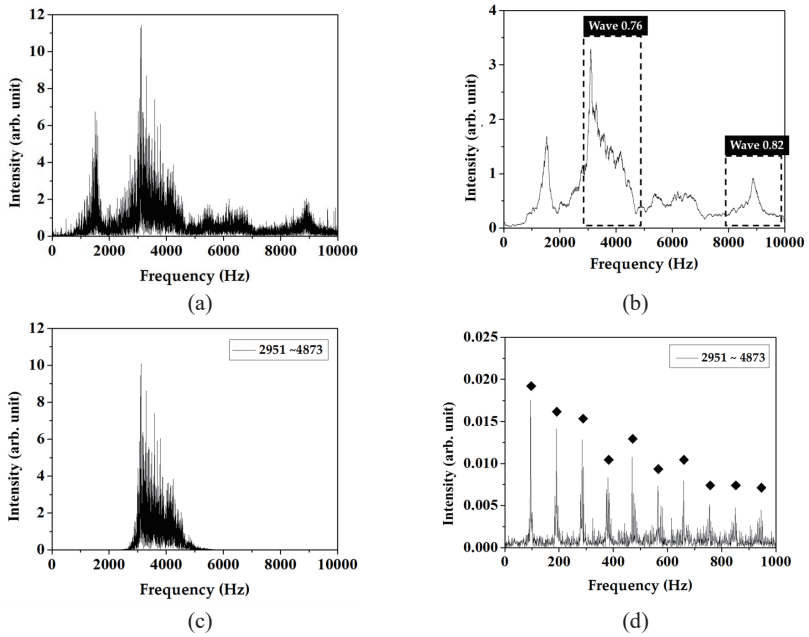

Fig. 26. Validation of bearing damage diagnostic system: frequency domain signal of (a) damaged outer ring bearing operating at 800 rpm, (b) applied SMA treatment and automatic mode selection, (c) after bandpass filtering, and (d) CEEO signal demodulation.

Table 6
Characteristic frequencies of damaged bearings at three different speeds and locations (calculated values are the same as those in Table 2).

Rotation speed (rpm)	Damaged location	Calculated value (Hz)	Identified value (Hz)	Percentage error (%)
2400	Inner ring	395.2	396.1	0.23
	Roller	233.6	231.2	1.03
	Outer ring	284.8	284.3	0.18
1600	Inner ring	263.5	264.0	0.19
	Roller	155.7	154.6	0.71
	Outer ring	189.9	189.0	0.47
800	Inner ring	131.7	131.2	0.38
	Roller	77.9	77.3	0.77
	Outer ring	94.9	94.5	0.42

have a very small error compared with the calculated values. This demonstrates the excellent performance of the automatic recognition system in automatic modal identification and modal demodulation.

6. Conclusions

To resolve the issue of mode identification in vibration detection, we combined the image recognition spectrum and the traditional diagnostic method to develop a new model for the

diagnosis of the health status of the bearing. We trained the model using YOLOv7 on 666 raw spectrum images for 50 epochs, and a prediction precision of 97% was achieved. The model integrates AI to accurately identify and analyze vibration modes, thereby enhancing the prediction accuracy of vibration modes and damages. The model's performance can be further improved with more data. The model can be embedded in a production system for vibration detection to eliminate the need to stop production lines and rely on experts for analysis. A comparison of CEEO with wavelet transforms revealed that CEEO requires significantly fewer computational resources while yielding analogous results. This reduction in computational demand leads to decreases in hardware requirements and diagnostic equipment costs. Furthermore, the integration of edge computing capabilities and automatic detection and warning systems into the model facilitates fully automated operation and real-time monitoring.

7. Future Work

In the future, we aim to integrate CEEO with statistical methods and deploy the system on an embedded platform, allowing it to be installed on various equipment. This approach will eliminate the reliance on professional personnel for spectrum analysis in mechanical diagnostics. Frontline operators will be able to utilize this system to assess whether a bearing requires maintenance, thereby minimizing equipment damage, reducing personnel injuries, and preventing associated losses.

Acknowledgments

The authors are grateful to Y. P. Luo, T. C. Wu, W. Y. Tzeng, T. H. Meen, and C. T. Ho for their help.

References

1 A. Rai and S. H. Upadhyay: Tribol. Int. **96** (2016) 289. https://doi.org/10.1016/j.triboint.2015.12.037
2 Report on Wind Turbine Subsystem Reliability ─ A Survey of Various Databases. https://www.nrel.gov/docs/fy13osti/59111.pdf (accessed April 2024).
3 J. Mathew and R. J. Alfredson: J. Vib. Acoust. **106** (1984) 447. https://doi.org/10.1115/1.3269216
4 M. Tadina and M. Boltežar: J. Sound Vib. **330** (2011) 4287. https://doi.org/10.1016/j.jsv.2011.03.031
5 P. D. McFadden and J. D. Smith: Tribol. Int. **17** (1984) 3. https://doi.org/10.1016/0301-679X(84)90076-8
6 R. B. W. Heng and M. J. M. Nor: Appl. Acoust. **53** (1998) 211. https://doi.org/10.1016/S0003-682X(97)00018-2
7 J. Maclntyre, J. Tait, S. Kendal, and P. Smith: WIT Trans. Inf. Commun. Technol. **6** (1944) 37. https://doi.org/10.2495/AI940021.
8 R. Kaur and S. Singh: Digit. Signal Process. **132** (2023) 103812. https://doi.org/10.1016/j.dsp.2022.103812
9 A. Vijayakumar and S. Vairavasundaram: Multimedia Tools Appl. **83** (2024) 83535. https://doi.org/10.1007/s11042-024-18872-y
10 C. Y. Wang, A. Bochkovskiy, and H. Y. M. Liao: Proc. Conf. Computer Vision and Pattern Recognition (IEEE, 2023) 7464–7475.
11 O. E. Olorunshola, M. E. Irhebhude, and A. E. Evwiekpaefe: J. Comput. and Soc. Inform. **2** (2023) 1. https://doi.org/10.33736/jcsi.5070.2023
12 X. Zheng, P. Yang, K. Yan, Y. He, Q. Yu, and M. Li: Eng. Appl. Artif. Intell. **133** (2024) 108087. https://doi.org/10.1016/j.engappai.2024.108087
13 R. Yan, Z. Shang, H. Xu, J. Wen, Z. Zhao, X. Chen, and R. X. Gao: Case Stud. Mech. Syst. Signal Process. **200** (2023) 110545. https://doi.org/10.1016/j.ymssp.2023.110545

14 N. G. Nikolaou and I. A. Antoniadis: NDT & E Int. **35** (2002) 197. https://doi.org/10.1016/S0963-8695(01)00044-5
15 M. Liang and H. Faghidi: Expert Syst. Appl. **41** (2014) 7223. https://doi.org/10.1016/j.eswa.2014.05.026
16 M. Heydarian, T. E. Doyle, and R. Samavi: IEEE Access **10** (2022) 19083. https://doi.org/10.1109/ACCESS.2022.3151048
17 R. Padilla, W. L. Passos, T. L. B. Dias, S. L. Netto, and E. A. B. da Silva: Electronics **10** (2021) 279. https://doi.org/10.3390/electronics10030279
18 J. L. Herlocker, J. A. Konstan, L. G. Terveen, and J. T. Riedl: ACM Trans. Inf. Syst. **22** (2004) 5. https://doi.org/10.1145/963770.963772
19 R. Padilla, S. L. Netto, and E. A. B. da Silva: Proc. Int. Conf. Syst. Signals Image Process. (IEEE, 2020) 237–242. https://doi.org/10.1109/IWSSIP48289.2020.9145130
20 P. Henderson and F. Vittorio: Proc. Asian Conf. Comput. Vis. (ACCV, 2016). https://doi.org/10.48550/arXiv.1607.03476
21 Y. Tsujimoto, Y. Miki, S. Shimatani, and K. Kiyono: Phys. Rev. E **93** (2016) 553304. https://doi.org/10.1103/PhysRevE.93.053304
22 Y. Zhuang, L. Chen, X. S. Wang, and J. Lian: Proc. 27th Int. Conf. Distrib. Comput. Syst. (IEEE, 2007). https://doi.org/10.1109/ICDCS.2007.83
23 Design and Fabrication of Prototype System for Early Warning of Impending Bearing Failure: https://ntrs.nasa.gov/api/citations/19720020851/downloads/19720020851.pdf (accessed April 2024).
24 S. A. McInerny and Y. Dai: IEEE Trans. Educ. **46** (2003) 149. https://doi.org/10.1109/TE.2002.808234
25 M. Liang and I. Soltani Bozchalooi: Mech. Syst. Signal Process. **24** (2010) 1473. https://doi.org/10.1016/j.ymssp.2009.12.007
26 Y. T. Sheen: J. Sound Vib. **303** (2007) 538. https://doi.org/10.1016/j.jsv.2007.01.035
27 Y. T. Su, M. H. Lin, and M. S. Lee: J. Sound Vib. **165** (1993) 455. https://doi.org/10.1006/jsvi.1993.1270
28 P. D. McFadden and J. D. Smith: J. Sound Vib. **96** (1984) 69. https://doi.org/10.1016/0022-460X(84)90595-9
29 Y. T. Sheen: Meas. **43** (2010) 912. https://doi.org/10.1016/j.measurement.2010.03.011

About the Authors

Chiu-Chang Chen received his B.S. and M.S. degree in mechanical engineering from Southern Taiwan University of Science and Technology in 2013 and 2015, respectively. He is currently pursuing his Ph.D. degree at National Formosa University. His research interests include industrial Internet of Things (IIoT), vibration signal processing and analysis, and embedded system research. (d1081102@gm.nfu.edu.tw)

Jenn-Kai Tsai received his B.S., M.S., and Ph.D. degrees from the Department of Physics of National Sun Yat-Sen University in 1996, 1998, and 2003, respectively. He is currently a professor in the Department of Electrical Engineering at National Formosa University, Yunlin, Taiwan. His current research interests focus on the wide-bandgap semiconductor nanoscale structure, dye-sensitized and perovskite solar cells, sensors, IoT, and so forth. (tsaijk@nfu.edu.tw)

Wei-Ming Huang received his B.S. and M.S. degrees from the Department of Electronic Engineering of National Formosa University in 2021 and 2023, respectively. His research focuses on dye-sensitized solar cells. (11060119@gm.nfu.edu.tw)

Yan-Feng Wang received his B.S. and M.S. degrees from the Department of Electronic Engineering of National Formosa University in 2021 and 2023, respectively. His research focuses on deep learning, particularly in the areas of image recognition, image processing, and the application of advanced deep learning techniques to enhance visual data analysis and interpretation. His work aims to leverage cutting-edge neural network architectures to improve the accuracy and efficiency of image-based tasks. (11060110@gm.nfu.edu.tw)